ANL/CP--71633

DE91 008832

Large aperture CCD x-ray detector for protein crystallography using a fiberoptic taper

M.G. Strauss, E.M. Westbrook, I. Naday, T.A. Coleman, M.L. Westbrook and D.J. Travis

Argonne National Laboratory, Argonne, Illinois 60439

R.M. Sweet

Brookhaven National Laboratory, Upton, New York 11973

J.W. Pflugrath

Cold Spring Harbor Laboratory, Cold Spring Harbor, New York 11724

M. Stanton

Brandeis University, Waltham, Massachusetts 02254

ABSTRACT

A detector with a 114 mm aperture, based on a charge-coupled device (CCD), has been designed for x-ray diffraction studies in protein crystallography. The detector was tested on a beamline of the National Synchrotron Light Source at Brookhaven National Laboratory with a beam intensity greater than 10^9 x-ray photons/s. A fiberoptic taper, an image intensifier and a lens demagnify, intensify, and focus the image onto a CCD having 512x512 pixels. A detective quantum efficiency (DQE) of 0.36 was obtained by evaluating the statistical uncertainty in the detector output. The dynamic range of a 4x4 pixel resolution element, comparable in size to a diffraction peak, was 10^4. The point-spread function shows FWHM resolution of approximately 1 pixel, where a pixel on the detector face is 160 μm. A complete data set, consisting of forty-five 1° rotation frames, was obtained in just 36 s of x-ray exposure to a crystal of chicken egg-white lysozyme. In a separate experiment, a lysozyme data set consisting of 495 0.1° frames, was processed by the MADNES data reduction program, yielding symmetry R-factors for the data of 3.2-3.5%. Diffraction images from crystals of the myosin S1 head (a=275 Å) were also recorded. The Bragg spots, only 5 pixels apart, were resolved but were not sufficiently separated to process these data. Changes in the detector design which will improve the DQE and spatial resolution are outlined. The overall performance showed that this type of detector is well suited for x-ray scattering investigations with synchrotron sources.

1. INTRODUCTION

A central task in experimental protein crystallography is to measure x-ray diffraction patterns of crystals. From these measurements, the 3-dimensional structure of the protein within the crystal can be determined. A diffraction pattern is obtained when x rays are scattered from a crystal as shown in Fig. 1. The function of a detector in these experiments is to produce a record of the diffraction pattern, from which the position and intensity of the Bragg spots can accurately be determined. Protein crystals diffract weakly; typically less than 0.1% of the incident x-ray beam scatters from the crystal. Because the diffraction yield is low, protein diffraction experiments are time consuming, and they benefit considerably from the use of intense synchrotron x-ray beams. In addition, protein crystals degrade when exposed to x rays. The damage can be minimized by acquiring the data rapidly with a brilliant synchrotron x ray source and a detector that is not count-rate limited.

X-ray detectors may be classified into two categories: counters and integrators. Counters, like multiwire gas proportional counters, require a finite processing time for each incident photon that is counted, and hence their count-

---

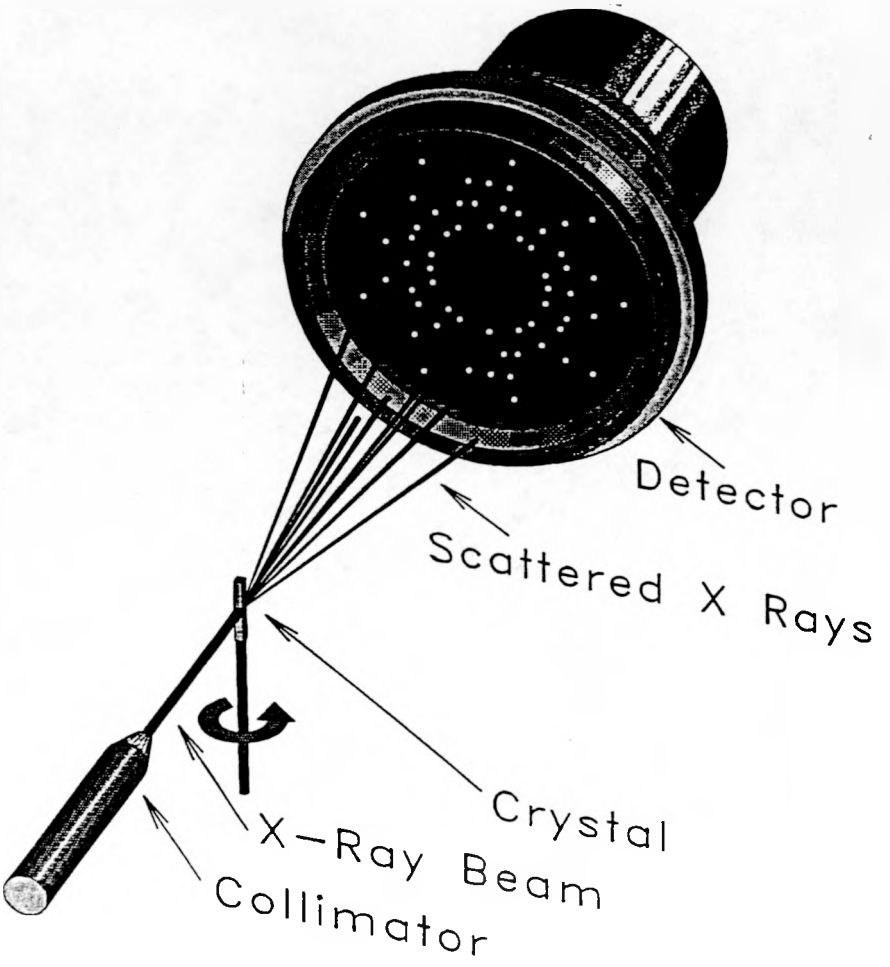

Fig. 1 Diffraction image formation. Collimated x rays scattered from a rotating protein crystal form a diffraction pattern on the detector face.

ing rate is limited. Integrators, like x-ray film and CCDs, integrate, without processing, all the photons incident during an exposure, and therefore have no counting rate limitation. X-ray film has been, and still is, a widely used detector in protein crystallography, because it is inexpensive and easily used. However, film has several limitations.[1] Its high noise level (fog) limits the dynamic range and saturation effects result in nonlinearity. In addition, the need for off-line film development and readout is a major disadvantage. It precludes on-line monitoring of the experiment, and when many diffraction images are acquired, processing the film is time consuming and effort intensive. The recently introduced image plates[2,3] are far superior to x-ray film in terms of dynamic range, linearity, and efficiency, but these are not realtime detectors either.

A CCD in which the x-rays are detected directly in the sensor would be the ideal realtime detector if it were not for the radiation damage produced. To circumvent this limitations the sensor is illuminated indirectly by using a phosphor screen to convert the x-ray photons into visible light photons and the resulting image is then optically focused onto the CCD. Integrating realtime detectors based on this principle but using silicon intensifier target (SIT) vidicon camera tubes have been in use for many years.[4-7] The emergence of CCDs for scientific applications, with their clear advantage with respect to noise and dynamic range over vidicon tubes,[8] has stimulated us[9-11] and others[12-16] to develop CCD-based detectors.

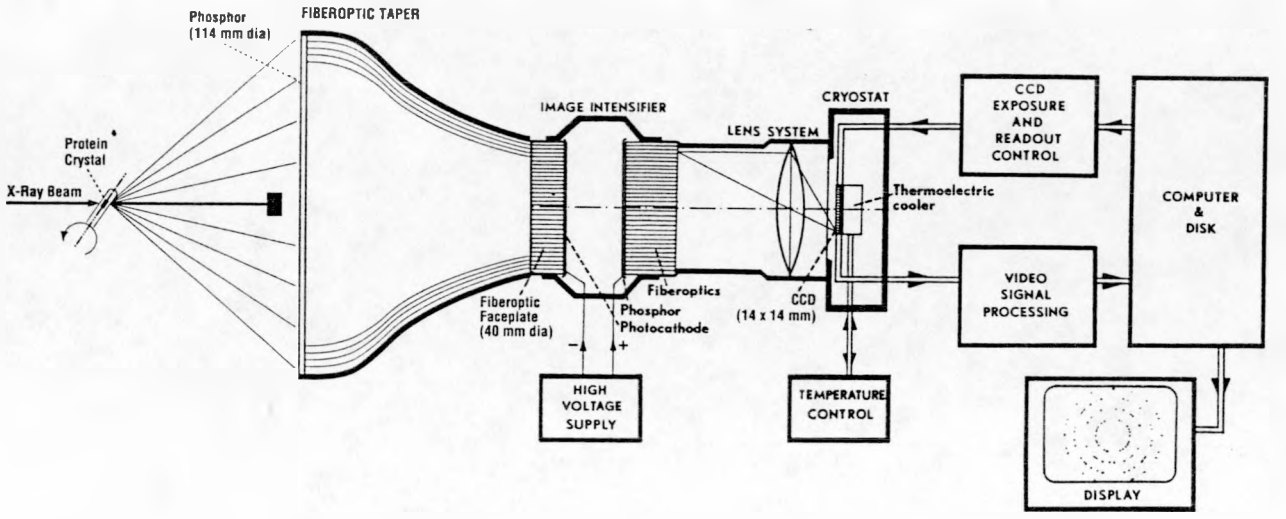

Fig. 2. Schematic diagram of the CCD-based detector showing its use in recording diffraction images from protein crystals. An image produced on the phosphor screen is demagnified, intensified, and focused on a 512x512 pixel CCD. The CCD data are read out into the computer and displayed on the video monitor. A complete data set consists of a sequence of frames obtained while the crystal is rotating in the x-ray beam.

In this paper we describe the design of the prototype detector developed at Argonne and report results of tests performed on beamline X12-C of the National Synchrotron Light Source (NSLS) at Brookhaven National Laboratory.[17] These tests were conducted to evaluate the performance of a CCD-based detector with intense x-ray beams, to characterize this particular detector, and to identify design aspects needing improvement.

2. DETECTOR DESIGN

The principal configuration of the detector is dictated by several key requirements. In order to resolve closely spaced Bragg spots, the detector must be placed several centimeters from the sample crystal (Fig. 1). Moreover, x-rays striking the crystal produce not only Bragg spots but also an undesirable diffuse background. This background is proportional to the inverse square of the crystal-to-detector distance. Hence, placing the detector at some distance from the crystal is important in order to achieve an acceptable signal-to-background ratio. In view of these spacing requirements, if the detector is to subtend a reasonably large solid angle it should have a large aperture of at least 100 mm and a spatial resolution of 0.1 mm or less. These figures are based on a typical setup of an experiment where the x-ray beam diameter is in the range of 0.1-0.3 mm. Thus, the aperture of the required detector clearly exceeds the dimensions of current CCD sensors, and therefore the diffraction images on the face of the detector must be reduced to the size of the CCD. This electro-optical reduction is the most critical design aspect of this type of detector as it should be realized with minimum distortion, noise generation, and loss of brightness.[18]

Our detector system is shown schematically in Fig. 2. X-rays scattered from the rotating crystal produce diffraction images on the phosphor screen (Gd_2O_2S:Tb) attached to the large end of the fiberoptic taper (114 mm dia.). The phosphor is covered with a light-tight window (not shown in Fig.1). The small end of the taper (40 mm dia.) is coupled to a 2-stage, electrostatically focused (generation I) image intensifier. The images are reduced approximately 3-fold by the fiberoptic taper and transmitted through the image intensifier to the lens system. The lens system demagnifies the image 2-fold and focuses it on the 512x512 pixel CCD. Thus, with a total of 6-fold demagnification the 13.8x13.8 mm^2 CCD projects an area on the detector face of 83x83 mm^2, i.e., each 27x27 μm^2 CCD pixel is projected as a detector pixel of 162x162 μm^2.

The CCD is mounted inside a vacuum chamber and is thermoelectrically cooled to -40° C. An electronically operated optical shutter (not shown in Fig. 2) is mounted between the lens and cryostat window. An

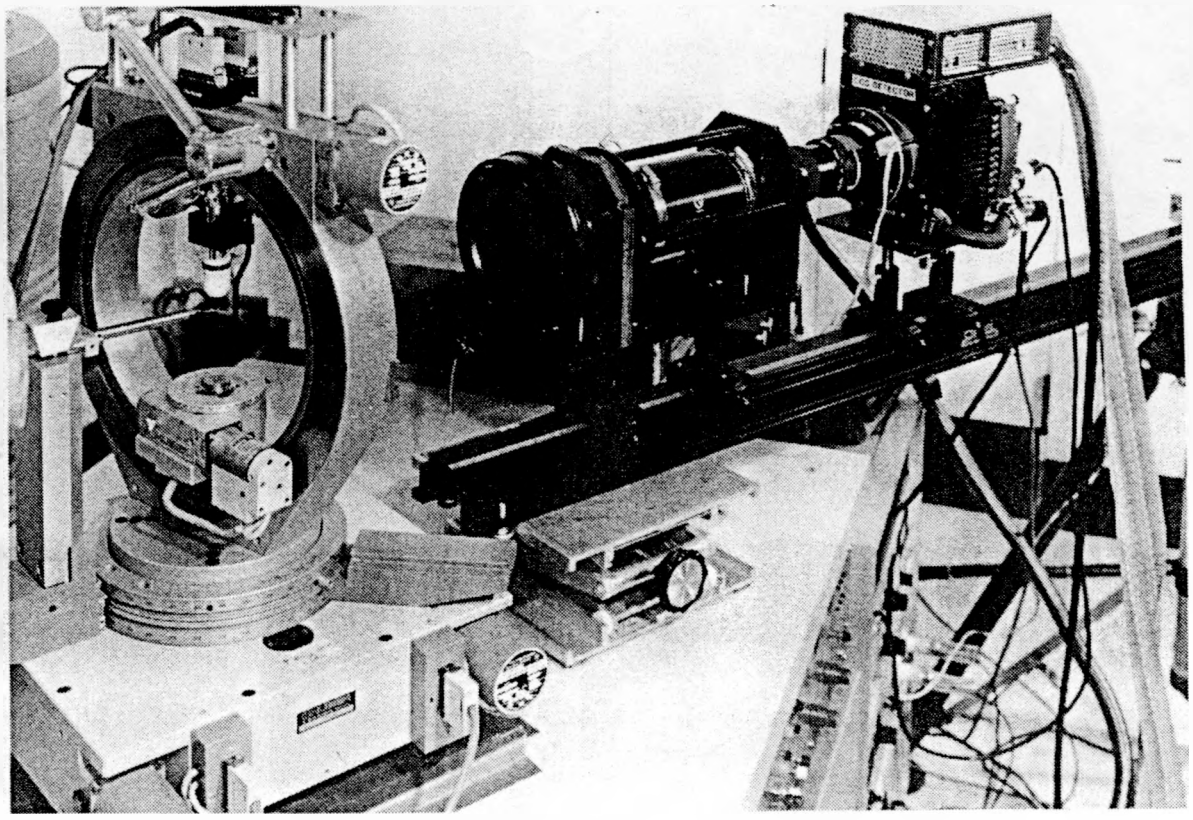

Fig. 3. Prototype detector (right) shown installed at a rotating anode x-ray generator. The front phosphor screen on the fiberoptic taper is covered by a light-tight window consisting of double-aluminized Mylar. The x-ray collimator (left) is pointing at the protein crystal mounted in the center of the goniostat.

x-ray shutter (not shown) is positioned in the path of the x-ray beam in front of the collimator.

A photograph of the detector, installed at a rotating anode x-ray generator, is shown in Fig. 3. The detector (right) is mounted on an optical bench where the large fiberoptic taper followed by the image intensifier are coupled via the lens system to the CCD chamber containing the readout circuits on top. The x-ray collimator (left) is pointing at the protein crystal which is mounted in the center of the goniostat. Data is acquired by executing the following sequence of operations: exposure, CCD readout, and save image data to disk. During the exposure the x-ray shutter and optical shutter are open and the crystal is rotated at a constant velocity through an incremental angle. All these operations are controlled by the CCD controller.[11] The exposure time, the number of exposures to be taken, and the frame size are specified via the computer.

The CCD signals are amplified by a video amplifier with a gain of 25, extracted by the correlated double sampling technique,[19] digitized by a 12-bit ADC, and transferred in parallel to the computer. Using the specified CCD sensitivity of 0.45 μV/e- gives a full-well capacity of 890×10^3 e- and 217 electrons/ADC unit (e-/ADU). The maximum readout rate is 3.2 μs/pixel or 0.85 s/frame, where a frame is 512x512 pixels. This requires a data transfer rate of 0.6 MB/s which was beyond the capabilities of our DMA interface. In the experiments reported here we therefore operated at ~7 s/frame. The specifications of the principal components of the detector system are listed in the Appendix.

3. DETECTOR PERFORMANCE

The accuracy with which one can record a diffraction pattern is dependent on several performance measures of which the principal ones are discussed below.

3.1 Dynamic range

Dynamic range is defined as the maximum detector signal-to-noise ratio, where both are integrated over a resolution element. The total noise is a composite of the dark-current noise (including the image intensifier EBI), readout noise, and ADC quantization error (±½ LSB). The typical RMS deviation in pixel values observed in dark exposures (1-30 s) was 0.7 ADU (150 e-). We believe that the ADC quantization error accounts for most of this deviation. When the resolution element is a pixel, we observed a dynamic range of 6,000. However, in the context of this work a resolution element is not a pixel but the area occupied by a diffraction peak. The signals in these pixels add algebraically whereas the noise adds in quadrature. Therefore, with judiciously selected peak bounds, the signal-to-noise ratio of the peak will be higher than that of a single pixel. For the case where a peak occupies an area of 4x4 pixels, we obtained a dynamic range of 10,000.

3.2 Linearity

The linearity of the detector was measured at NSLS by varying the exposure time over a 15:1 range with the x-ray shutter and monitoring the 11-keV x-ray beam intensity incident on the detector with the calibrated ion chamber. The integral of the image in the detector as a function of the integrated input for different exposure times gives the linearity transfer function. The output vs. input response of the detector, with a regression line fitted through the data points, is shown in Fig. 4. The response is linear over the full range.

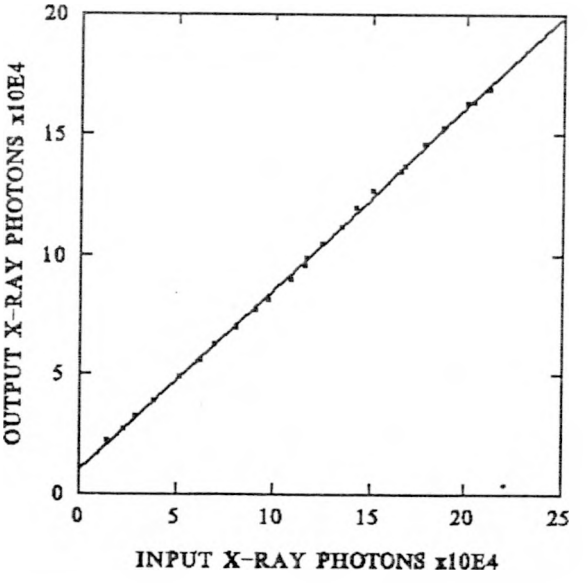

Fig. 4. Detector output vs. input transfer function, showing linearity of response measured with an 11-keV x-ray beam. The measurement was made by varying the exposure time with the x-ray shutter. The input was measured with a calibrated transmission ion chamber. The Y intercept corresponds to a DC offset of 20 ADU/pixel. The coordinates are in units of 10^4 x-ray photons.

3.3 Detective quantum efficiency

The precision with which data are recorded by an imaging detector is affected by the signal-to-noise ratio. Detective quantum efficiency (DQE) is the figure of merit that relates precision and signal-to-noise ratio.[20] It is defined as:

$$DQE = \frac{(signal/noise)^2_{out}}{(signal/noise)^2_{in}}. \qquad (1)$$

The uncertainty σ_o in the output signal S_o can be shown to be:

$$\frac{\sigma_o}{S_o} = [(DQE)\ S_i]^{-1/2}, \qquad (2)$$

where S_i is the observed input signal. When DQE = 1, the detector is said to be photon limited because $\sigma_o/S_o = \sigma_i/S_i = S_i^{-1/2}$ as determined by photon statistics. When DQE < 1 due to a reduced signal/noise at the output, σ_o/S_o is greater than σ_i/S_i. Thus, in order to estimate the uncertainty in intensity measurements of diffraction spots, DQE must be known.

We evaluated DQE by estimating the contribution to the statistical uncertainty σ_o/S_o of each component in the signal chain. A diagram of the signal chain is shown in Fig. 5. The average light yield of the phosphor was measured at 70 light photons (Lph) per incident x-ray photon. The yield appears low because absorption losses in the TiO_2 reflector on the phosphor were not accounted for in the yield measurements and because of inefficient coupling of the phosphor screen to the fiberoptic taper. Separate measurements were made of the image intensifier gain (G) and light transfer efficiency (LTE) of the taper and lens using green light (wavelength ~550 nm). The quantum efficiency (QE) was taken from the CCD specifications. The calculated signal strength corresponding to an input of one 11 keV x-ray photon is shown at each stage. The overall detector conversion gain of 66 e-/Xph was obtained from a separate measurement.

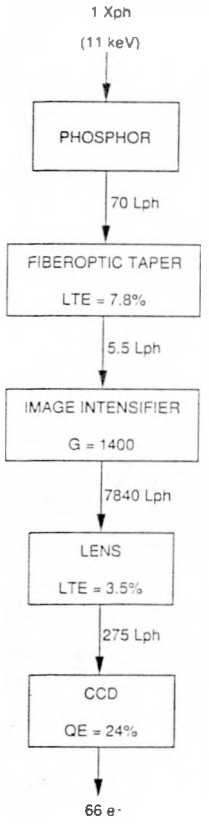

Fig. 5. Diagram showing the propagation of the optical signals through the detector components. The average yield of the phosphor per incident x-ray photon (Xph) is 70 light photons (Lph). With a light-transfer efficiency (LTE) of 7.8%, the signal out of the fiberoptic taper is 5.5 Lph. With a gain (G) of 1400 in the image intensifier, the signal is amplified to 7840 Lph. Through the lens, the signal is reduced to 275 Lph, which in turn create (with a quantum efficiency QE of 24%) 66 electrons (ė-) in the CCD.

In the present discussion the variance in the CCD output signal is assumed to be equal to the sum of the variances of the input signal, of the signals at each detector stage, and the variance due to random noise in the detector. The dominant variances in the signal chain are those associated with the weakest signals. The minimum signal is at the photocathode of the first stage of the image intensifier. The quantum efficiency of the photocathode (S-20 Extended Red) is 11.5%, and therefore the average yield is 0.63 photoelectrons per x ray photon. In subsequent stages the signal is amplified, ultimately yielding 66 e-/Xph in the CCD.

Assuming that all variances in the signal chain obey, or can be approximated by, Poisson statistics and considering only the variances at the output of the taper ($1/S_t$) and at the image intensifier photocathode ($1/S_{pc}$), the fractional variance in the output signal S_o can be calculated as follows:

$$\frac{(\sigma_o)^2}{(S_o)^2} = \frac{1}{S_i} + \frac{1}{S_t} + \frac{1}{S_{pc}} + \frac{(\sigma_n)^2}{(S_o)^2}, \qquad (3)$$

where $(\sigma_n)^2$ is the mean-square deviation in the measured random noise (Sec. 3.1) and it is assumed that $S_o = S_i$. From Fig. 5 $S_t = 5.5S_i$ and from above $S_{pc} = 0.63S_i$. Substituting these into eq. (3) and solving for DQE with eq. (2) gives

$$DQE = 1/[2.77 + (\sigma_n)^2/S_o]. \qquad (4)$$

For large signals where $[(\sigma_n)^2/S_o] << 2.77$, the uncertainty is limited by the efficiency of the front-end optical components which result in $DQE = 1/2.77 = 0.36$.

The precision expected in Bragg peaks observed in diffraction patterns was evaluated from the data obtained in the linearity measurement (Sec. 3.2). The fractional statistical uncertainty for the input and output signals was calculated as discussed above. Plots of σ_o/S_o vs. S_o (top) and σ_i/S_i vs. S_i are shown in Fig. 6. The uncertainty at the output is higher than that at the input by $(DQE)^{-1/2} = 1.67$ [eq. (2)].

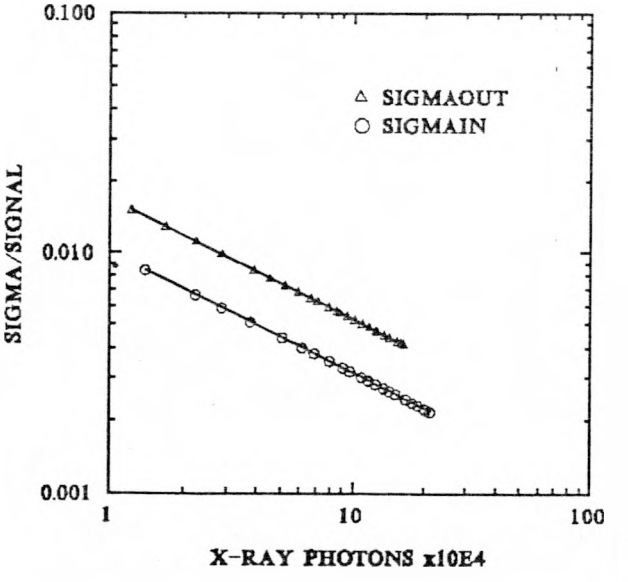

Fig. 6. Estimated relative statistical standard deviation in the input (○) and output (▲) signals obtained in the linearity measurement shown in Fig. 4. It was calculated with eq. (2) where for the input DQE = 1 and for the output DQE = 0.36. The relative standard deviation at the output is higher than that at the input by $(DQE)^{-1/2} = 1.67$. The X coordinate is in units of 10^4 x-ray photons.

3.4 Spatial resolution

The point-spread function was obtained by imaging the x-ray beam through a 50-μm pinhole in a platinum plate placed in line with the center of the detector 6 cm from the front face. The profile along a pixel row is shown in Fig. 7. The pinhole diameter was not deconvoluted from these profiles. The true FWHM resolution cannot be determined directly from this response function (top) because it is on the order of 1 pixel (160 μm). The intrinsic FWHM resolution of the Trimax 2 phosphor screen was measured at ~65 μm. The detector point-spread function (bottom) decays to 0.1% of maximum at 4-5 pixels from the center. The point spread function along a column is very similar to that along a row (Fig. 7), showing no evidence of blooming when the center pixel was at 90% of full well. There is also no evidence of veiling glare, i.e., slowly decaying, extended tails of the point-spread function starting at 1-2% of maximum. Veiling glare is attributed to scattering in the image intensifier[21] and/or lens and CCD.[18]

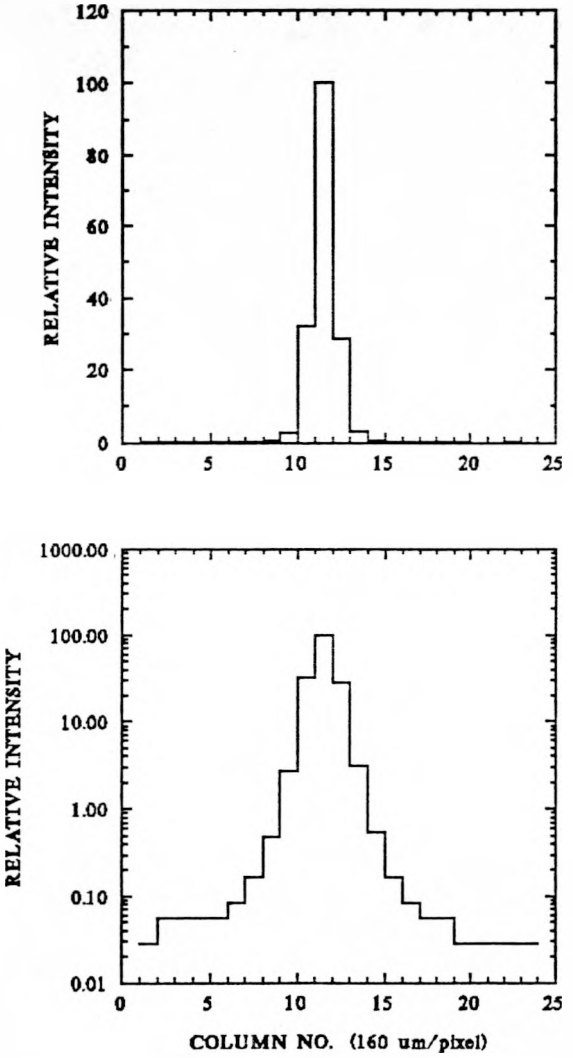

Fig 7. Point-spread function along a pixel row shown with a linear scale (top) and logarithmic scale (bottom). It was obtained by imaging an 11-keV x-ray beam through 50-μm pinhole in platinum plate. The FWHM resolution is approximately 1 pixel. The response is down to 0.1% of maximum at 4-5 pixels from the center.

3.5 Uniformity and distortion

The spatial uniformity of response was measured by exposing the detector to a uniform x ray flood from an ^{55}Fe x-ray point source (5.9 keV, assumed to be isotropic) placed in front of the detector. The resulting flood image exhibited a lower response off center due to vignetting caused by the lenses and geometric distortion caused by the image intensifier. A diffraction image obtained by scattering 11-keV x rays from a protein crystal mounted in the same

position as the ^{55}Fe source can be expected to exhibit the same nonuniformity as the flood image. We therefore used the flood image in correcting the nonuniformity in the diffraction images. The off-center nonuniformity, as well as the CCD pixel-to-pixel nonuniformity, and the fiberoptic taper transmission nonuniformity, were corrected by applying intensity normalization factors computed from the flood image. Experimentally observed diffraction images are first corrected by subtracting the dark image and then by multiplying each pixel value by its normalization factor.

The diffraction image also suffers from spatial distortion, particularly pincushion distortion from the image intensifier. To correct for spatial distortions a precision test pattern, (consisting of an array of holes drilled into a brass plate) was imaged on the detector with an ^{55}Fe x-ray source. Comparison of the known pattern in the brass plate against the image of the pattern recorded by the detector permitted computation of displacement coefficients for each pixel. These coefficients were used to correct spatial distortion in the diffraction images by rebinning the data in the appropriate pixels. A raw "brass plate" image is shown in Fig. 8. The reduced intensity off-center is primarily due to vignetting similar to that observed in the flood image. Pincushion distortion, caused by the image intensifier, is also present. Fig. 9 shows the brass plate image after intensity normalization and correction for geometric distortion. This image is free of spatial distortion as well as intensity nonuniformity.

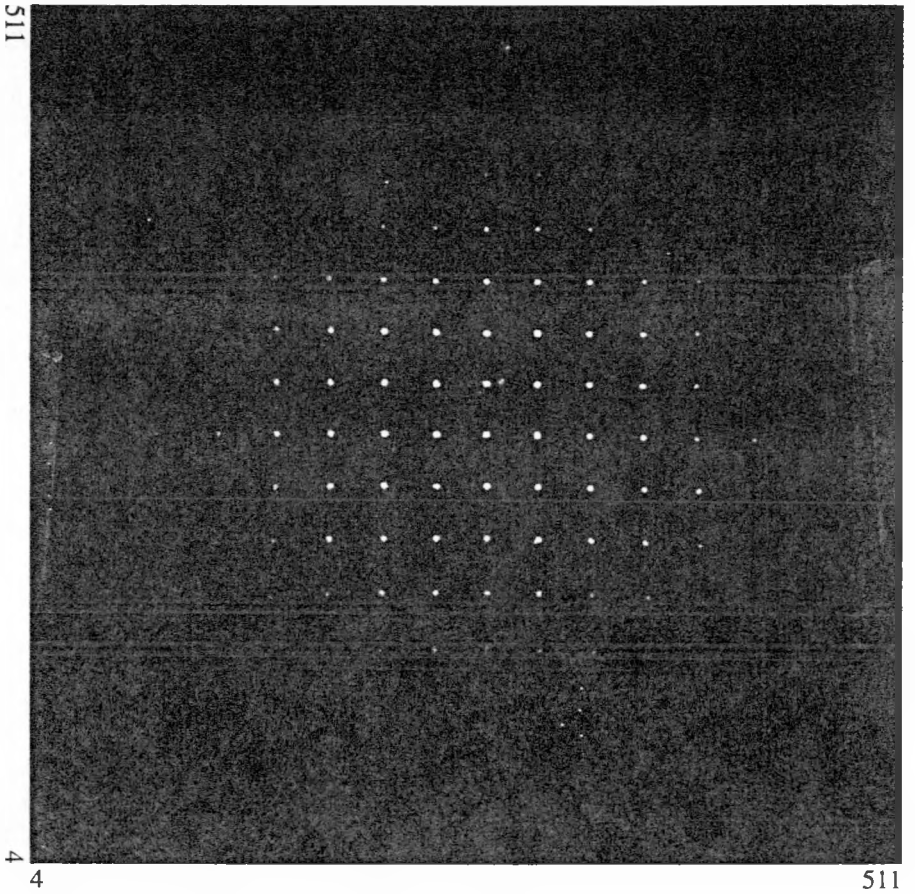

Fig. 8. Image of a precision test pattern (an array of holes in a brass plate) used for correcting spatial distortion in the diffraction images caused by the image intensifier and fiberoptic taper. The reduced intensity off center is primarily due to vignetting caused by the lenses and pincushion distortion caused by the image intensifier.

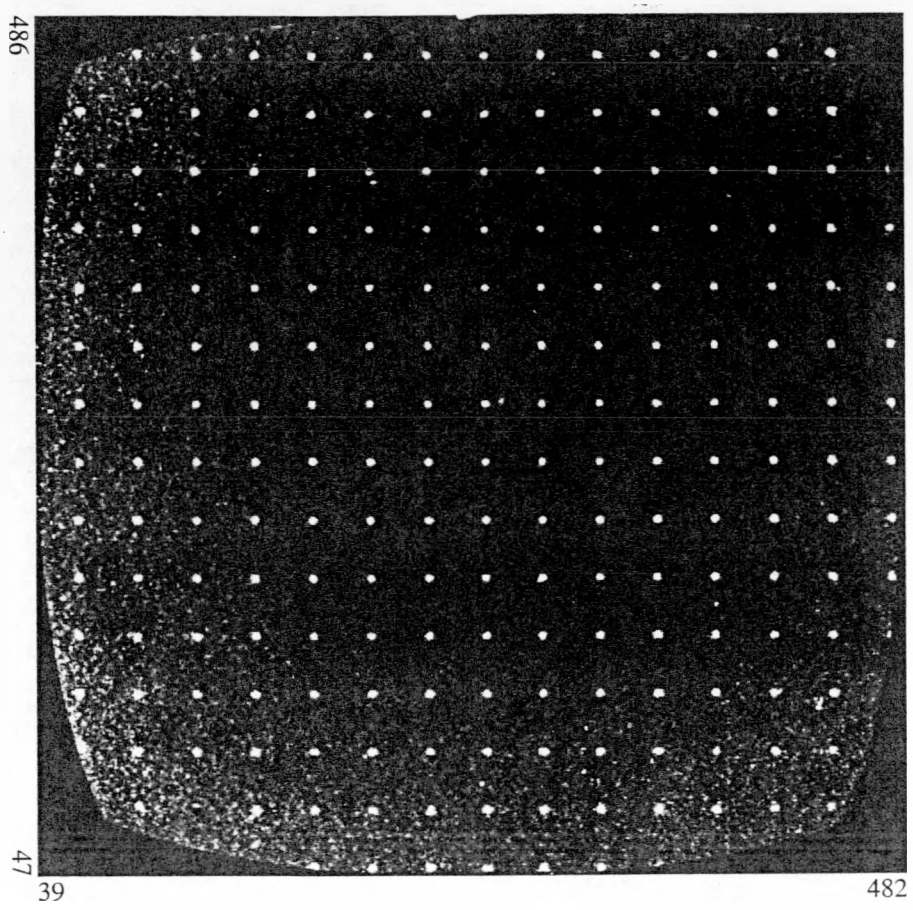

Fig. 9. Image of the brass-plate test pattern shown in Fig. 8, corrected for intensity nonuniformity and geometric distortion. This image has uniform response and is free of spatial distortion.

4. DIFFRACTION EXPERIMENTS

The digital output of each CCD pixel is proportional to the number of x ray photons incident on the corresponding area of the detector face. However, the pixel output is measured in arbitrary ADC units (ADUs). To determine the number of Xph per ADU, we measured the x-ray beam intensity with a photomultiplier tube with an attached phosphor, the anode current of the tube had been calibrated in terms of Xph/s. From the known intensity of the beam, the exposure time, and the integral of the image in the CCD detector, we obtained the number of Xph/ADU.

The ability of the detector to record accurate diffraction images was evaluated by collecting data on tetragonal crystals of chicken egg-white lysozyme and on orthorhombic crystals of the S1 head of myosin.[22]

4.1 Lysozyme crystals

The detector was mounted on an optical bench 14 cm from the sample crystal (Fig. 1). A complete lysozyme data set, consisting of 45 1.0° -frames, was recorded in a total of 36 s of x-ray exposure. The x-ray rate on the detector exceeded 8×10^6 Xph/s. Each frame contained, on the average, 6×10^6 Xph. A sample frame, obtained in 0.8 s, is shown in Fig. 10 after dark-image subtraction and intensity normalization, Spot A (row 190) is the brightest unsaturated spot in the image (84% of maximum), containing over 5×10^4 Xph. It was observed with a calculated precision

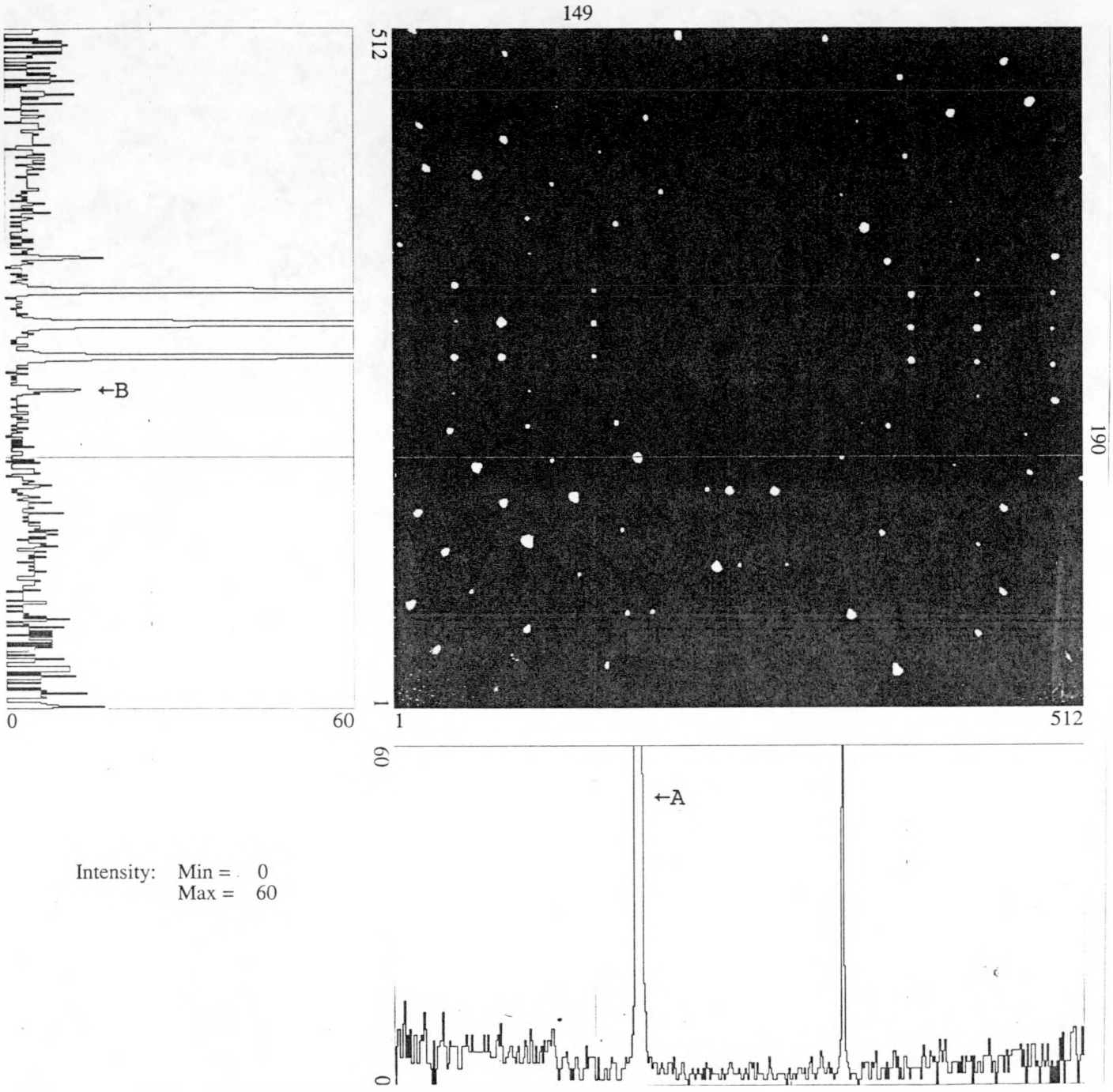

Fig. 10. Diffraction image of a chicken egg-white lysozyme crystal. Data were integrated over a crystal rotation of 1° during a 0.8 s exposure. This image is part of a complete data set of 45 frames collected in just 36 s of x-ray exposure. The x-ray rate on the detector exceeded 8×10^6 photons/s giving an average of 6×10^6 x-ray photons per frame. Spot A is the brightest unsaturated peak, containing more than 5×10^4 photons. Spot B is the weakest peak discernible containing 200 photons. The intensity is in ADC units, where 1 ADU = 3.3 Xph.

$\sigma_o/S_o = 0.73\%$ [eq. (2)]. Spot B (column 149) is the weakest spot discernible (0.3% of maximum), containing 200 Xph. It was observed with a precision of 15%.

To further characterize this detector, a lysozyme data set of 495 frames was acquired and evaluated. Each frame was integrated over a rotation angle of 0.1° in 1.5 s and contained an average of 3.4×10^6 Xph. The complete data set was recorded in 12 min of crystal exposure to x rays (the total data acquisition time was considerably longer because the computer data-transfer rate necessitated a slow readout of 40 Kpixel/s). The data sets were processed by a modified version of MADNES[23] -- a computer program for processing single crystal diffraction data from area detectors. The symmetry R-factor, "R-symm," is the standard figure of merit for protein crystallographic data; it was used for estimating the precision with which symmetry-related Bragg spots were reproduced at different points on the detector and in different data frames. 3,496 reflections of 1,187 unique data were measured to a maximum resolution of 3.6 Å (data extending to 3.1 Å were measured in the corners of the image). The symmetry R-factors ranged from 3.5% at the center of the detector to 3.2% at 3.6 Å resolution.

4.2 Myosin head crystals

Data on myosin head crystals[22] were of particular interest because of their large unit cell dimensions and hence closely spaced diffraction spots. The myosin crystals have cell dimensions of 275 Å, 99.5 Å, and 125 Å. In order to resolve the Bragg spots, we moved the detector as far as possible from the crystal (23 cm). The central region of a data frame obtained with a 0.32 mm diameter collimator, over a 1° crystal rotation, and a 52 s x-ray exposure is shown in Fig. 11. The spots along column 404 are spaced 5 pixels apart, 0.81 mm on the detector face. They are clearly separated but are not fully resolved, as seen in the profile on the left; the valleys between the spots do not completely return to the background level. Using a collimator with a diameter of 0.15 mm did not appear to improve the spot resolution appreciably. From the column point-spread function we estimate that less than half of the rise in the valley is due to the detector response. The remainder may be accounted for by non-instrumental factors such as beam divergence and mosaic spread.

5. DISCUSSION

The most demanding aspect of the design of this detector is the faithful reduction of a large diffraction image on the detector face to the size of a CCD. This reduction is accomplished here with a fiberoptic taper and a lens system. The primary purpose of the image intensifier is to offset the light losses in these two components. This optical chain in front of the CCD limited the performance of the detector. It lowered the DQE, distorted the image, introduced substantial nonuniformity of response, and increased the detector noise. These limitations could, in a future design, be avoided or ameliorated by using an array of large area CCDs thereby eliminating or reducing the requirements for image demagnification.

The results of the experiments described above brought to light several other design shortcomings. In the present detector implementation it was expedient to attach a ready made phosphor screen to the fiberoptic taper, which resulted in reduced light yield. In a future design the phosphor could be deposited directly on the fiberoptic taper thereby increasing the signal-to-noise ratio and, in turn, the DQE. The ADC quantization error ($\pm\frac{1}{2}$ LSB or $\pm$ 1/8192) was a major source of noise which could be readily reduced by increasing the ADC precision from the present 12-bits. The spatial resolution is limited by the number of pixels in the present CCD (512^2). A CCD with 1024^2 pixels would project on the phosphor a pixel size of $80 \times 80\ \mu m^2$, comparable to the resolution of the phosphor (FWHM$\approx 65\ \mu m$). The limitation in the data transfer rate from the CCD to the computer has already been corrected by installing a faster DMA interface (DEC DRQ3B). With the maximum readout rate of $3.2\ \mu s$ / pixel the detector deadtime per frame of 512^2 pixels is now less than 1 s.

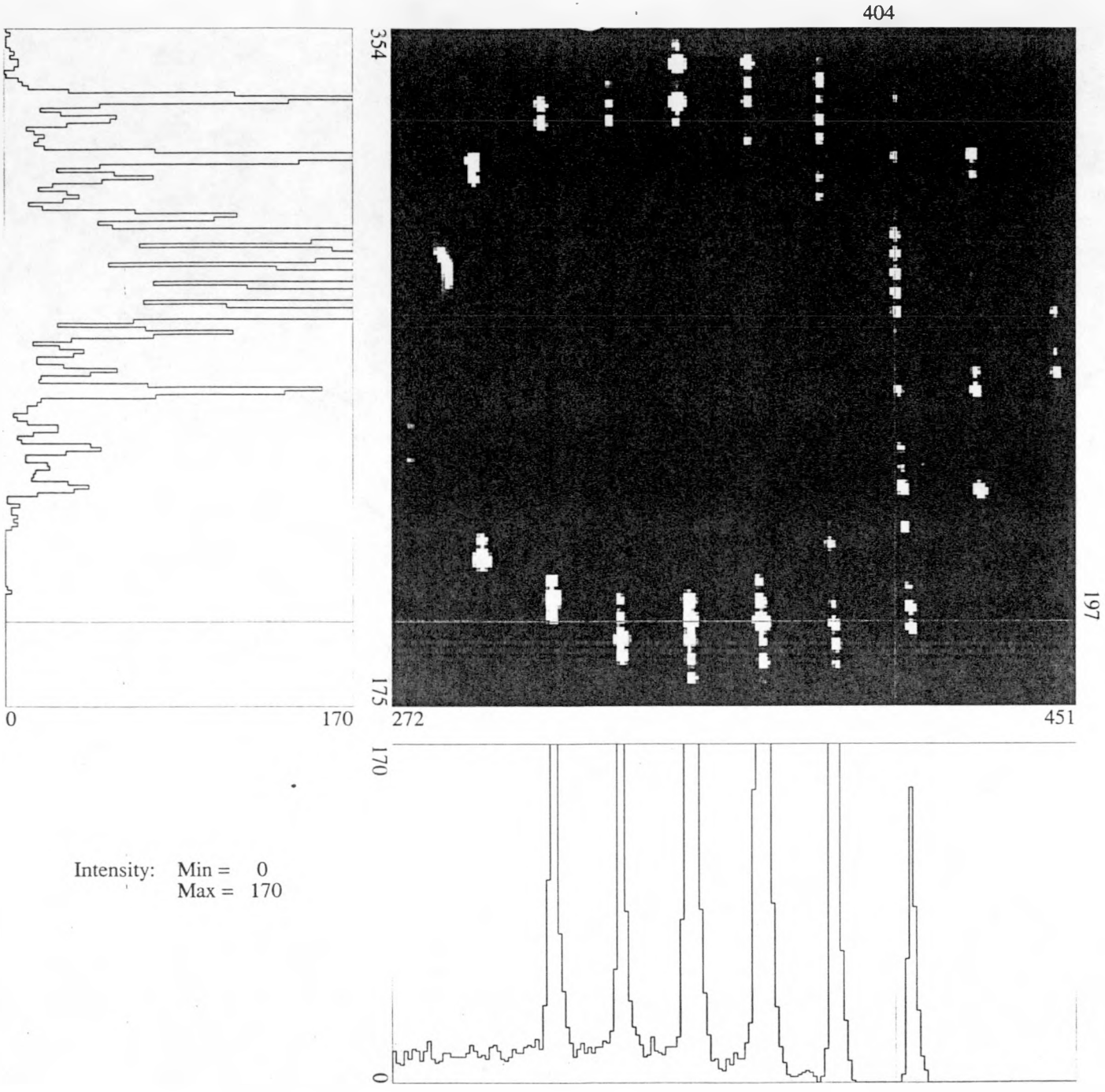

Fig. 11. Center region of a diffraction image of myosin S1 head crystal obtained by integrating over a 1° crystal rotation during a 52 s exposure; detector-to-crystal distance, 23 cm. The large unit cell dimensions of the crystal (a = 275 Å) result in closely spaced Bragg spots. The spots along column 404 are clearly separated but not fully resolved, as seen in the profile (left), where the valleys between the peaks do not return all the way to the background level. The intensity is in ADC units, where 1 ADU = 3.3 Xph.

6. CONCLUSION

A CCD-based detector with a 114-mm aperture has been characterized and shown to be able to record high quality protein diffraction data with synchrotron x rays. A nearly complete data set from a lysozyme crystal was recorded in a total of 36 s of x-ray exposure. The R-symm obtained in several experiments with lysozyme crystals were 3-4%. The DQE was 0.36 for Bragg peaks ranging down to 1% of the maximum peak. The dynamic range was 10^4. The FWHM spatial resolution was on the order of 1 pixel, i.e., approximately 160 μm on the detector face.

The basic concept of a large area CCD based detector for protein crystallography with synchrotron x rays was clearly validated. Notwithstanding the high quality of the experimental results, several noteworthy changes in design are being considered for the next detector. These should improve the statistical precision, uniformity of response, and spatial resolution.

A realtime integrating detector that instantly displays the diffraction images provides prompt feedback which has proved invaluable in setting up experiments and monitoring their progress. Unlike film and imaging plates, the data acquired with such detectors are in the computer as soon as the exposure of a frame is completed, permitting online data reduction and inspection of results.

The performance of the detector and the experimental results convinced us that such a detector promises to find wide applications in x-ray diffraction research at synchrotron facilities.

6. ACKNOWLEDGMENTS

We gratefully acknowledge the assistance of T.E. Hentsch, S.A. Reinke, M.R. Kroll, and M.D. Anderson. I.S. Sherman made significant contributions in the early stages of the detector development. W.C. Phillips of Brandeis University provided a critical review of the manuscript and made valuable suggestions which have been incorporated. This work and beamline X12-C at the National Synchrotron Light Source at Brookhaven National Laboratory are supported by the U.S. Department of Energy, Office of Health and Environmental Research.

7. APPENDIX

SPECIFICATIONS OF PRINCIPAL DETECTOR COMPONENTS

COMPONENT	MANUFACTURER (Model)	SPECIFICATIONS
Phosphor screen	3M, St. Paul, Minn. (Trimax 2)	Gd_2O_2S:Tb (P43), layer thickness 50μm, grain size <4 μm, wavelength 545 nm, TiO_2 reflector.
Fiberoptic taper	Schott Fiber Optics, Southbridge, Mass.	Dia. 116:40 mm, length 100 mm, fiber dia. 25 μm (large end), NA 1.0 (small end), EMA.
Image intensifier	Varo, Garland, Texas (1268)	Gen.I, 2 stage, dia. 40:40 mm, photocathode S-20 ER, output phosphor P-20.
Lens	Nikon, Tokyo, Japan (Nikkor)	2 lenses "nose-to-nose": 105 mm, f/2.5; 50 mm, f/1.2, magnification 0.5.
Electronic shutter	Melles Griot, Rochester, N.Y. (04IES003)	Aperture 34.9 mm, response ~3 ms, delay 5 ms.
Cryostat	Marlow Industries, Dallas, Texas	Chamber: thermoelectric & fan cooled, vacuum ~10^{-5} Torr, quartz window. CCD: 3-stage thermoelectric cooled -40°C.
CCD	Tektronix, Beaverton, Oregon (TK512M)	Full frame 512x512 pixels, pixel size 27 μm x 27 μm, front illuminated, 0.45 μV/-e.
CCD Controller	Argonne Nat'l Lab., Argonne, Ill. (CD105)	20 MHz clock, max. readout 5 Mpixel/s, computer controlled.
CCD signal processor	Argonne Nat'l Lab., Argonne, Ill. (MA281)	Video amp. gain 25, correlated double sampling, max. readout 3.2 μs/pixel.
ADC	Burr Brown, Tucson, Ariz. (803)	12 bits, 1.5 μs, 10 V input.
Computer	Digital Equipment Corp., Maynard, Mass. (VAXstation II/GPX)	1 MIPS, Memory 13 MB, 3 disks @150 MB, DMA transfer ~0.2 frames/s (interface DEC DRV11).

7. REFERENCES

1. S.M. Gruner, "Time-Resolved X-ray Diffraction of Biological Materials," *Science,* vol. 238, pp. 305-312, 1987.

2. J. Miyahara, K. Takahashi, Y. Amemiya, N. Kamiya and Y Satow, "A New Type of X-ray Area Detector Using Laser Stimulated Luminescence," *Nucl. Instr. and Meth.,* vol. A246, pp. 572-578, 1986.

3. D. Bilderback, K. Moffat, J. Owen, B. Rubin, W. Schildkamp, D. Szebenyi, B. Smith Temple, K. Volz and B. Whiting, "Protein Crystallographic Data Acquisition and Preliminary Analysis Using Kodak Storage Phosphor Plates," *Nucl. Instr. and Meth.,* vol. A266, pp. 636-644, 1988.

4. U.W. Arndt, "X-ray Television Area Detectors," *Nucl. Instr. and Meth.,* vol. 201, pp. 13-20, 1982.

5. U.W. Arndt and G.A. In't Velt, "Further Developments of an X-ray Television Detector," *Adv. Electr. Electr. Phys.,* vol. 74, pp. 285-296, 1988.

6. K. Kalata, "A General Purpose, Computer-Configurable Television Area Detector for X-ray Diffraction Applications," *Meth. in Enzymology,* vol. 114, pp. 486-510, 1985.

7. K. Kalata, W.C. Phillips, M. Stanton and Y. Li, "Development of a Synchrotron CCD-Based Area Detector for Structural Biology," *Proc. SPIE,* vol. 1345, pp. 270-280, 1990.

8. S.M. Gruner, "CCD and Vidicon X-ray Detectors: Theory and Practice," *Rev. Sci. Instr.,* vol. 60, pp. 1545-1551, 1989.

9. M.G. Strauss, I. Naday, I.S. Sherman, M.R. Kraimer and E.M. Westbrook, "CCD-Based Synchrotron X-ray Detector for Protein Crystallography--Performance Projected from an Experiment," *IEEE Trans. Nucl. Sci.,* vol. NS-34(1), pp. 389-395, 1987.

10. I. Naday, M.G. Strauss, I.S. Sherman, M.R. Kraimer and E. M. Westbrook, "Detector with Charge-Coupled Device Sensor for Protein Crystallography with Synchrotron X-rays," *Opt. Eng.,* vol. 26, pp. 788-794, 1987.

11. M.G. Strauss, I. Naday, I.S. Sherman, M.R. Kraimer, E.M. Westbrook and N.J. Zaluzec, "CCD Sensors in Synchrotron X-ray Detectors," *Nucl. Instr. and Meth.,* vol. A266, pp. 563-577, 1988.

12. R.L. Dalglish, V.J. James and G. Tubbenhauer, "A Two-Dimensional X-ray Diffraction Pattern Sensor Using a Solid State Area Sensitive Detector," *Nucl. Instr. and Meth.,* vol. 227, pp. 521-525, 1984.

13. E.F. Eikenberry, S.M. Gruner and J.L. Lowrance, "A Two-Dimensional X-ray Detector with a Slow-Scan Charge-Coupled Device Readout," *IEEE Trans. Nucl. Sci.,* vol. NS-33(1), pp. 542-545, 1986.

14. R.H. Templer, S.M. Gruner and E.F. Eikenberry, "An Image-Intensified CCD Area X-ray Detector for Use with Synchrotron Radiation," *Adv. Electr. Electon Phys.,* vol. 74, pp. 275-283, 1988.

15. J. Widom and H.P. Feng, "High Performance X-ray Area Detector Suitable for Small-Angle Scattering, Crystallographic, and Kinetic Studies," *Rev. Sci. Instr.,* vol. 60, pp. 3231-3238, 1989.

16. H.F. Fuchs, D.Q. Wu and B. Chu, "An Area X-ray Detector System Based on a Commercially Available CCD-Unit," *Rev. Sci. Instr.,* vol. 61, pp. 712-716, (1990).

17. M.G. Strauss, E.M. Westbrook, I. Naday, T.A. Coleman, M.L. Westbrook, D.J. Travis, R.M. Sweet, J.W. Pflugrath and M. Stanton, "CCD-Based Detector for Protein Crystallography with Synchrotron X Rays," *Nucl. Instr. and Meth.* vol. A297, pp. 275-295, 1990.

18. H.W. Deckman and S.M. Gruner, "Format Alterations in CCD Based Electro-Optic X-ray Detectors," *Nucl. Instr. and Meth.,* vol. A246, pp. 527-533, 1986.

19. M.H. White, D.R. Lampe, F.C. Blaha and I.A. Mack, "Characterization of Surface Channel CCD Image Arrays at low Light Levels," *IEEE J. Solid State Circuits,* vol. SC-9, p.1, 1974.

20. S.M. Gruner, J.R. Milch and G.T. Reynolds, "Evaluation of Area Photon Detectors by Method Based on Detective Quantum Efficiency (DQE)," *IEEE Trans. Nucl. Sci.,* vol. NS-25(1), pp. 562-565, 1978.

21. J.D. Wiedwald and R.J. Hertel, "Veiling Glare in the ITT F4113 Image Intensifier," *Proc. SPIE,* vol. 981, pp. 154-160, 1988.

22. I. Rayment, U. of Wisc., Madison, private communication (1989).

23. A. Messerschmidt and J.W. Pflugrath, "Crystal Orientation and X-ray Pattern Prediction Routines for Area-Detector Diffractometer Systems in Macromolecular Crystallography," *J. Appl. Cryst.,* vol. 20, pp. 306-315, 1987.